Supporting information

Water- and Oxygen-Tolerant Phosphorescent Carbon Nitrides Enable Visual Hydrogel Biosensing

Zhuang Wang[a], Yongji Wang[d], Hong Yang[a], Kaiyuan Wang[a], Kaiqing Wu[a], Chenchen Wang[a], Jinpeng Cai[a], Songqin Liu[a], Chaofeng Huang[d], Yanfei Shen[b]*, Wei Wei[a]*, Yuanjian Zhang[a],[c]*

[a] Jiangsu Engineering Center of Smart Carbon-Rich Materials and Device, Jiangsu Province Hi-Tech Key Laboratory for Bio-Medical Research, School of Chemistry and Chemical Engineering, Southeast University, Nanjing 211189, China, E-mail: weiw@seu.edu.cn (W.Wei); Yuanjian.Zhang@seu.edu.cn (Y.Zhang)

[b] Center of Clinical Laboratory Medicine, Zhongda Hospital, and Jiangsu Provincial Key Laboratory of Critical Care Medicine, Medical School, Southeast University, Nanjing 210009, China
E-mail: Yanfei.Shen@seu.edu.cn (Y.Shen)

[c] Department of Oncology, Zhongda Hospital, Southeast University, Nanjing, 210009, China

[d] School of Chemistry and Chemical Engineering of Shihezi University, Shihezi, Xinjiang, 832000, China

Table of Content

1. Supplementary methods

1.1 Materials

Dicyandiamide (DCDA, 99%) and ethylene glycol (EG) were purchased from Sigma-Aldrich. Sodium chloride (NaCl), copper (II) chloride dihydrate ($CuCl_2·2H_2O$), magnesium chloride hexahydrate ($MgCl_2·6H_2O$), calcium chloride ($CaCl_2$), manganese (II) chloride tetrahydrate ($MnCl_2·4H_2O$), cadmium (II) chloride pentahydrate ($CdCl_2·5H_2O$), nickel (II) chloride hexahydrate ($NiCl_2·6H_2O$), iron (III) chloride ($FeCl_3$), hydrochloric acid (HCl), sodium hydroxide (NaOH), sodium chloride (NaCl), potassium chloride (KCl), and ethanol were purchased from Sinopharm Chemical Reagent Co., Ltd. (China). 1-butylimidazole (Imd), 1-butyl-3-methylimidazolium chloride (ImdCl), 1-butyl-3-methylimidazolium bromide (ImdBr), 1-butyl-3-methylimidazolium tetrafluoroborate ($ImdBF_4$), 1-butyl-3-methylimidazolium hexafluorophosphate ($ImdPF_6$), 1-butyl-3-methylimidazolium trifluoroacetate ($ImdAcF_3$), 1-ethyl-3-methylimidazolium chloride, 1-hexyl-3-methylimidazolium chloride, 1-octyl-3-methylimidazolium chloride, 1-decyl-3-methylimidazolium chloride, 1-ethoxyl-3-methylimidazolium chloride, 1-carboxymethyl-3-methylimidazolium chloride, sodium fluoride (NaF), sodium tetrafluoroborate ($NaBF_4$), sodium hexafluorophosphate ($NaPF_6$), sodium dicyanamide ($NaN(CN)_2$), sodium thiocyanate (NaSCN), Cysteine (99%), Glycine (99%), Dopamine (99%), Urea (99%), Ascorbic Acid (AA) (99%), BSA (96%), disodium ethylenediaminetetraacetate (EDTA-2Na, 99%) and agarose were purchased from Aladdin Chemistry Co., Ltd. (China). Ultrapure water (18.2 MΩ cm) used in all experiments was obtained from a Direct-Q 3 UV pure water purification system (Millipore, USA).

1.2 Measurements

X-ray power diffraction (XRD) patterns were measured using an Ultima IV (Rigaku, Japan). Fourier transform infrared (FT-IR) spectra were recorded using a Nicolet iS20 FT-IR spectrometer (Thermo Fisher, USA). The K-Alpha (Thermo Fisher, USA) was employed as the X-ray photoelectron spectrum (XPS) characterization with the peak of C1*s* (284.8 eV) as the reference for calibration. Matrix-free laser desorption ionization time-of-flight mass spectrometry (MFLDI-TOF MS) was performed using a Smart Beam II Nd:YAG/355 nm laser operating at 2,000 Hz (ultrafleXtreme, Bruker, Germany). Raman spectrum was measured by using a Xplora Raman microscope (λ=785nm, Horiba, France). The combustion elemental analysis was performed using an Elementar Vario EL III (Elementar, Hanau, Germany). The ^{1}H solid-state NMR spectrum was obtained using an AVANCE III 400 MHz WB solid-state NMR spectrometer (Bruker, Germany). Mass spectra were obtained using an Ultivo Triple Quadrupole LC-MS System (Agilent, USA). UV-vis absorption spectra were measured using a Cary100 UV-vis spectrophotometer (Agilent, USA). Fluorescence (Fluo) and phosphorescence (Phos.) spectra were measured using a Cary Eclipse fluorescence spectrophotometer (Agilent, USA). Variable-temperature phosphorescence spectra and lifetime decay spectra were measured using an FLS980 fluorescence spectrometer (Edinburgh Instruments, UK). Phosphorescence images were obtained using a Huawei Pura 70 Ultra with excitation using a 365 nm UV lamp. Transmission electron microscopy (TEM) images were obtained using a Tecnai G2 20 (FEI Company, USA). Thermogravimetric analysis (TGA) was conducted in N_2 atmosphere (100 mL min^{-1}) with a heating rate of 10 °C min^{-1} using an SDT-Q600 instrument (TA, USA). Contact angle tests were performed using a surface analyzer LSA-100 (Lauda, Germany). Femtosecond transient absorption spectra (fs-TAS) were obtained using a commercial transient absorption spectrometer (HELIOS, Ultrafast system) equipped with a 1 kHz Solstice (NewCorp.).

The phosphorescent quantum yield (QY) was acquired through peak-differentiation-imitating analysis[1-2] to distinguish the fluorescent and phosphorescent quantum yields according to their respective integrated area ratios identified in the steady-state photoluminescence (PL) spectra, following the equation:

$$\text{Phosphorescent QY}= \Phi\frac{A_{phos}}{A_{Fluo}+A_{phos}}$$

$A_{Fluo}\ and\ A_{phos}$ are the integral areas of fluorescence and phosphorescence, obtained from the steady-state PL spectrum.

The multiexponential Fluo. and Phos. decays are described by the following equation[3]:

$$\mathrm{I(t)}=\sum_x B_x e^{-\frac{t}{\tau_x}}$$

B_x and τ_x are the amplitudes and lifetimes of the individual components of the multiexponential decay profiles, respectively.

1.3 Computational methods

All density functional theory (DFT) calculations were performed using Gaussian 16 (revision C.02)[4]. Geometry optimizations were performed at the M06-2X/def2-SVP level, ensuring the absence of any imaginary frequencies[5]. Subsequently, electron excitations for the initial 50 excited states were determined via time-dependent DFT (TD-DFT) calculations using the M06-2X/def2-TZVP basis set, based on the previously optimized structures. The molecular orbitals were analyzed using the Multiwfn (revision 2.8(dev))[6]. Visualization of structures and molecular orbital images was achieved through Visual Molecular Dynamics (VMD, revision 1.9.3)[7].

1.4 Synthesis of materials

Preparation of bulk carbon nitride (bulk-CN).

Bulk carbon nitride was prepared through heating DCDA to 550 °C during 4 hours and kept at this temperature for 4 hours under air in a muffle furnace (Carbolite, U.K.)[8]. The final product was finely ground into a powder and used without further purification.

Preparation of microwave-assisted carbon nitride (CN_{mw})

Initially, 10 g of the DCDA precursor was dissolved in 100 mL of EG under stirring at 80°C for 20 min to form a true solution. Second, 5 mL of DCDA/EG solution was added to a 30 mL crucible and transferred into a microwave reactor (700 W, M1-L213B, 2.45 GHz, Midea, China)[9]. After irradiation for 120 s, the resulting pale-yellow solid was ground into a fine powder. Subsequently, the powder was washed three times each with ethanol and DI water to remove soluble oligomers. The residual sample was dried and denoted as CN_{mw}.

Preparation of CN-cy-Im and CN-cy-Im-Recal

Briefly, 20 g of the DCDA precursor was dissolved in 200 mL of EG and stirred at 80 °C for 30 min to form a true solution. Then, 0.105 g ImdCl was dissolved in 5 mL DCDA/EG solution under ultrasonic treatment for 20 min to form a uniform DCDA/EG-ImdCl mixture. After being placed at 80 °C for 30 min, the mixture was transferred into the microwave reactor and irradiated for 120 s. The resulting samples were finely ground into a powder and washed to obtain the final product, CN-cy-Im. Furthermore, CN-cy-Im was heated at a rate of 2.5 °C per minute to reach 400 °C and maintained for 30 min in air to prepare $CN_{mw}cal$.

Preparation of CN-cy-Im nanoparticles and nanosheets

First, 500 mg of CN-cy-Im was dispersed in a solvent composed of 40mL of DI water and 10mL of ethanol. The mixture was then mechanically ground by ball milling (YXQM-0.4L, Changsha Deco Equipment Co.,Changsha, China) for 12h at 300 rpm. Subsequently, gradient centrifugation was performed on the resulting slurry at various rotation rates to separate the CN-cy-Im with different sizes form microscale particles to nanosheets.

Preparation of CN-cy-ImdX (X = Br, AcF$_3$, BF$_4$, PF$_6$)

Similarly, 20 g of the DCDA precursor was dissolved in 200 mL of EG by stirring at 80 °C for 30 min to form a true solution. Then, 0.6 mM ImdBr, $ImdAcF_3$, $ImdBF_4$, and $ImdPF_6$ were added to 5 mL of the DCDA/EG solution under ultrasonic agitation for 20 min to form a uniform DCDA/EG-ImdX mixture. After being placed at 80 °C for 30 min, the mixture was transferred into the microwave reactor and irradiated for 120 s. The resulting samples were finely ground into a powder and washed to obtain CN-cy-ImdX.

Fabrication of time-dependent color-tunable RTP hydrogel

Briefly, 100 mg CN-cy-Im nanosheets were dispersed in 5 mL DI water with the addition of 50 mg agarose. The solution was then sonicated for 30 min to ensure complete mixing. Subsequently, the mixture was heated in a microwave for 10 min to dissolve the agarose and cooled to room temperature to form the CN-cy-Im hydrogel. Finally, the resulting hydrogel was tailored into various shapes and immersed in DI water.

1.5 Anion-exchange treatment of CN-cy-Im

300 mg CN-cy-Im was dissolved in 10 mL of DI water. Then, 10 mM NaF, $NaBF_4$, $NaPF_6$, $NaN(CN)_2$, and NaSCN were dissolved in the CN-cy-Im dispersion, which was subsequently stirred for 60 min. The resulting solution was centrifuged and washed thrice with DI water and ethanol. Finally, the samples were dried under vacuum at 60 °C for 24 h.

1.6 Cycle stability test

The CN-cy-Im solution was excited using a 365 nm UV lamp through optical silica fiber (Beijing NBET Technology Co., China). The shutter program was set up to realize each circle of excitation for 0.1 s and detection for 3s via H10682 photomultiplier (HAMAMATSU Photonics, Japan). The circle test was continuously carried out for 100 min to assess the phosphorescence stability of the CN-cy-Im nanosheets.

1.7 Phosphorescent responses of CN-cy-Im to different metal ions

Briefly, 600 μg CN-cy-Im nanosheets were added to 2 mL of Tris-HCl (10 mM, pH 7.4) containing various metal ions at different concentrations, and the mixed solution was stirred at room temperature for 60 min. Subsequently, phosphorescent spectra were recorded at a delay time of 1 ms.

1.8 Visual detection of Fe^{3+} based on phosphorescent CN-cy-Im hydrogel

Typically, the as-prepared CN-cy-Im hydrogel mentioned above was tailored into a fixed shape and immersed in 10 mL of Tris-HCl (10 mM, pH 7.4). The system was subsequently added with Fe^{3+} ions at different concentrations. The solution was then incubated at 37 °C for 20 min with shaking. Finally, different phosphorescence signals were tested, and the delayed emission was recorded.

2. Supplementary figures and tables

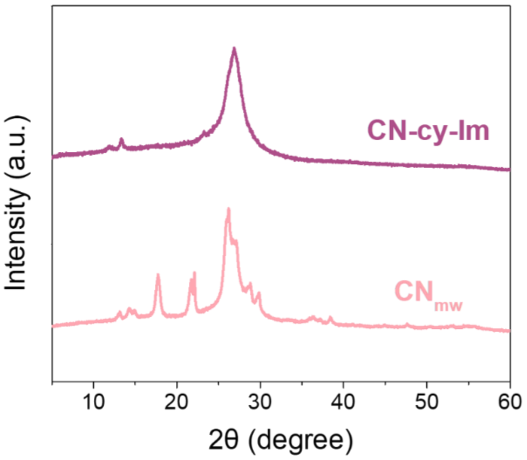

Fig. S1 XRD spectra of CN-cy-Im and CN$_{mw}$.

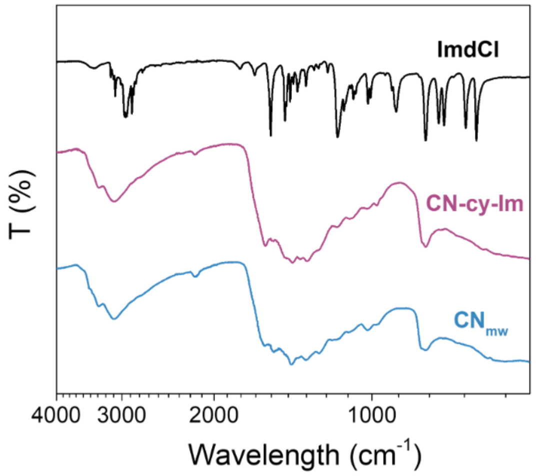

Fig. S2 FTIR spectra of ImdCl, CN-cy-Im and CN_{mw}.

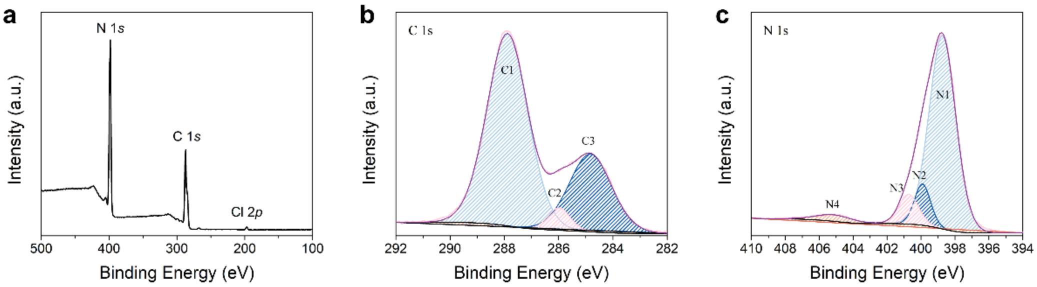

Fig. S3 XPS spectra of CN-cy-Im. (a) Survey spectrum, (b) C 1*s* spectrum, and (c) N 1*s* spectrum.

The survey spectrum first illustrated the existence of C, N, and Cl elements in CN-cy-Im (Fig. S3a). Moreover, the high-resolution C1*s* spectra (Fig. S3b) exhibited three main peaks at 288.0, 286.0, and 284.8 eV, ascribed to aromatic -C=N, $C-NH_x$ on the edges of heptazine units, and C-C bonds on the carbon chains of imidazolium, respectively[10]. The high-resolution N1*s* spectra (Fig. S3c) was deconvoluted into four peaks, including the sp^2 -C=N bonds in tri-s-triazine rings (398.7 eV), bridging N atoms, $N-(C)_3$ (400.0 eV), $-NH_x$ groups in the heptazine skeletons (400.8 eV) and charge effect (404.9 eV)[8].

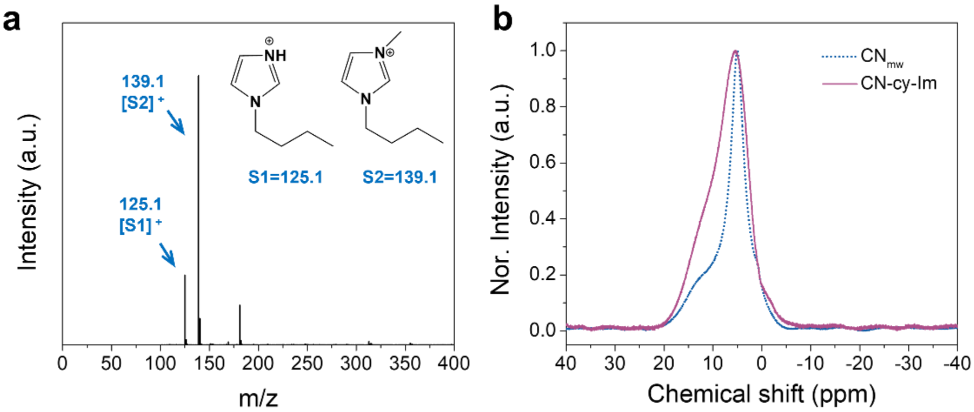

Fig. S4 (a) LC-MS spectrum of microwave-assisted condensation of single ImdCl. (b) Solid-state ^{1}H NMR spectroscopy of CN_{mw} and CN-cy-Im.

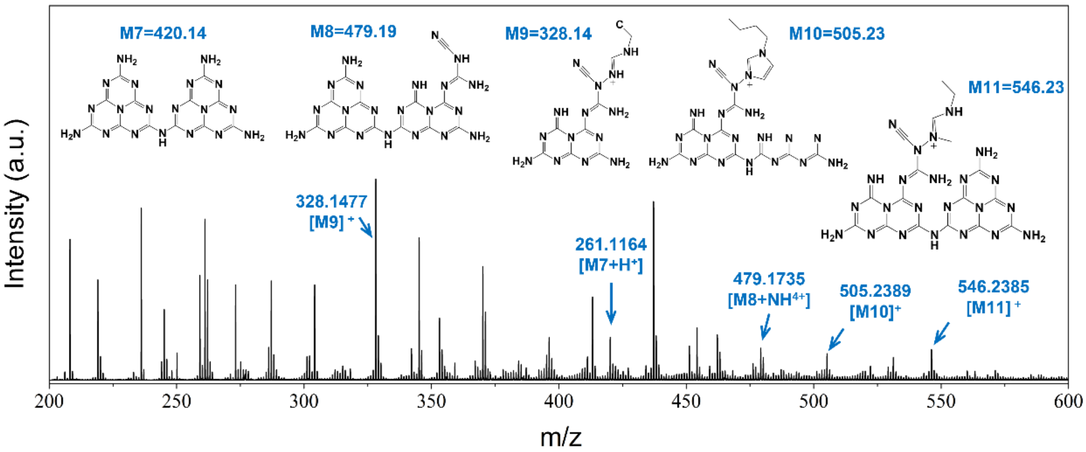

Fig. S5 LDI-TOF mass spectrum of CN-cy-Im with supplementary fragments assignment**.**

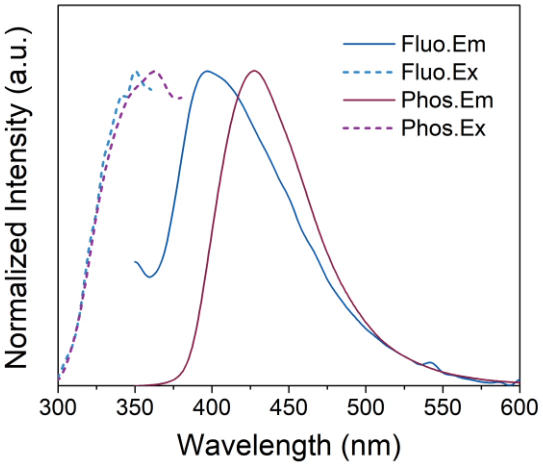

Fig. S6 Fluorescence and phosphorescence spectra of CN-cy-Im in the solid state (delay time = 1 ms).

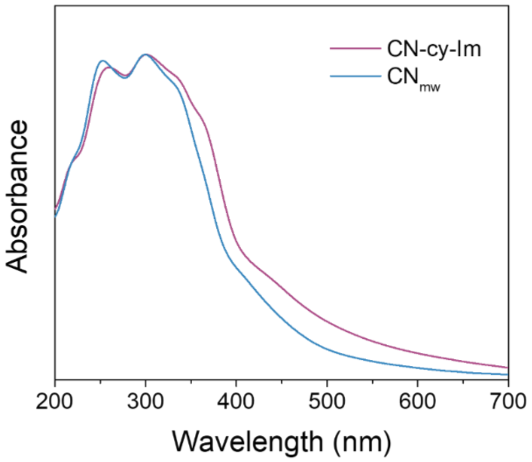

Fig. S7 UV-vis absorption spectra of CN-cy-Im and CN_{mw} in the solid state.

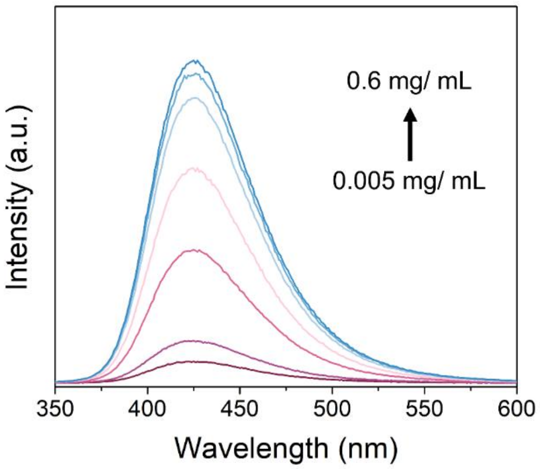

Fig. S8 Phosphorescence spectra of CN-cy-Im in aqueous solutions with different mass concentrations.

As shown in Fig. S8, the delayed emission intensity varied with different mass concentrations of CN-cy-Im nanosheets in aqueous solution, verifying the origin of RTP from CN-cy-Im in aqueous solution.

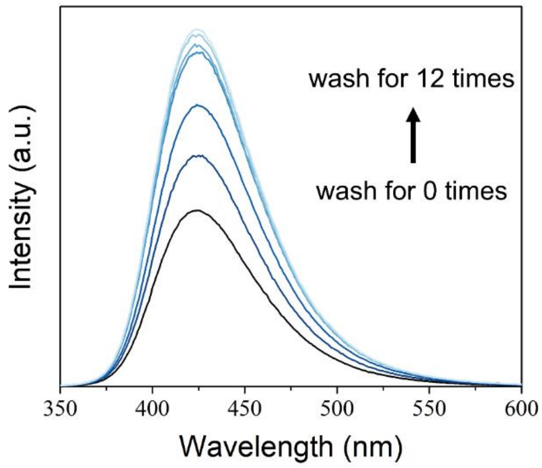

Fig. S9 Phosphorescence spectra of CN-cy-Im in aqueous solution with a concentration of 0.5 mg/mL after washing for different times.

Small fragments with a low degree of polymerization can be eliminated by solvent cleaning. Consequently, the intensity of aqueous delayed emission consistently increased as the ultrasonic washing time was extended, using deionized water and ethanol alternately (Fig. S9). This finding suggests that the aqueous RTP is linked to the polymeric carbon nitride structure rather than soluble molecules or low-molecular-weight oligomers.

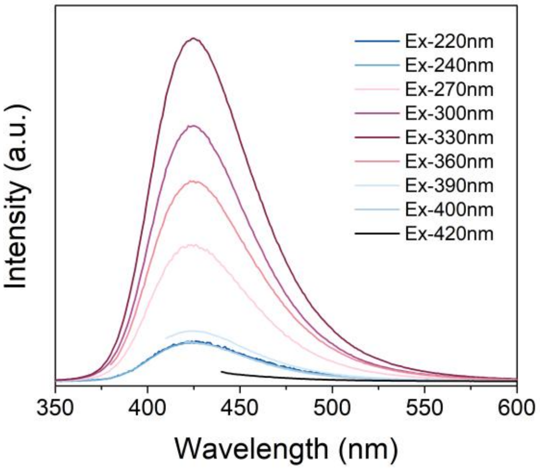

Fig. S10 Phosphorescence spectra of CN-cy-Im in aqueous solution under various excitation wavelengths.

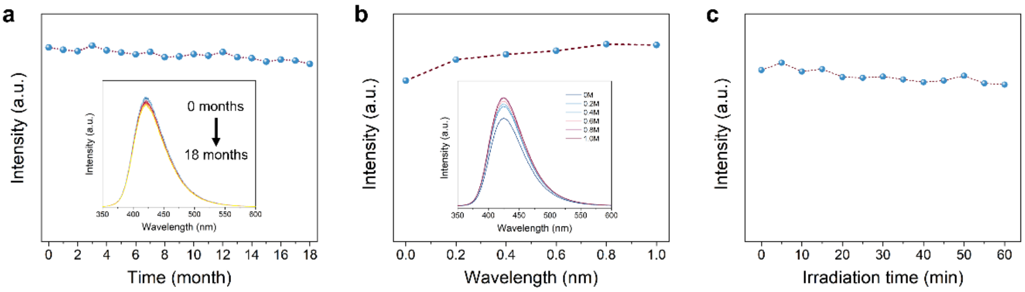

Fig. S11 Stability tests for CN-cy-Im in aqueous solution by measuring the phosphorescence intensity after (a) long-term storage, (b) introduction of different concentrations of NaCl and (c) long-lasting irradiation.

Various stability tests were performed under serial conditions. For instance, the aqueous phosphorescence intensity of the CN-cy-Im nanosheets remained almost unchanged (91.6 %) during storage in solution for 18 months (Fig. S11a), suggesting excellent storage stability. For reliable biological applications, aqueous phosphorescence emission was verified to be barely influenced by high concentrations of NaCl (Fig. S11b). In addition, CN-cy-Im exhibited good photostability in aqueous RTP emission, which hardly declined under continuous UV irradiation of UV light up to 60 min (Fig. S11c).

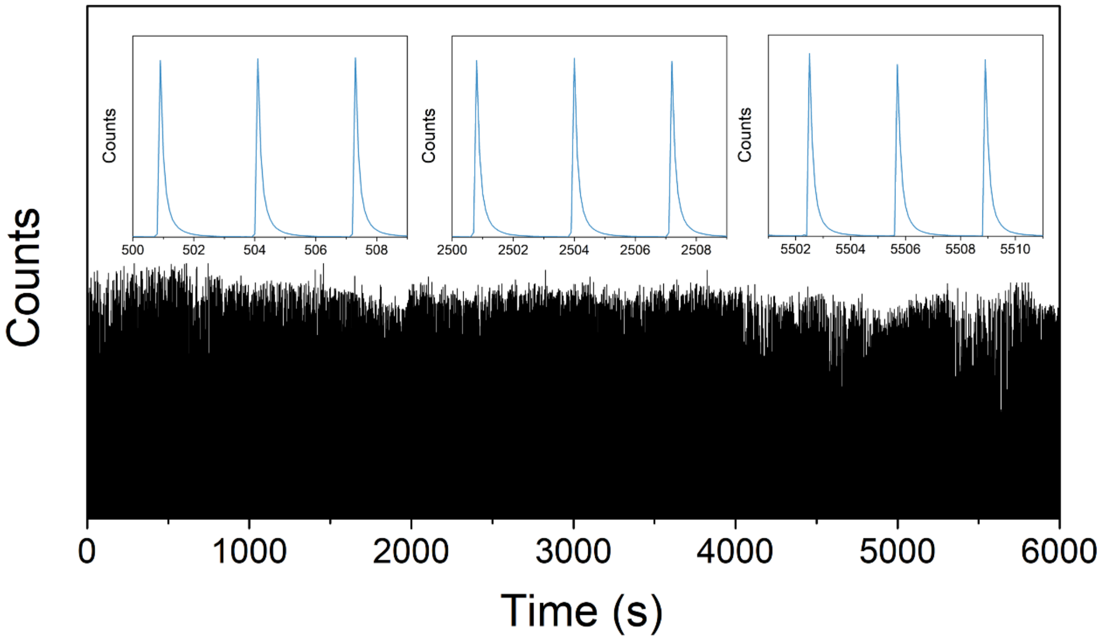

Fig. S12 Reliability test for CN-cy-Im with cyclic excitation and phosphorescence emission.

As illustrated in Fig. S12, CN-cy-Im exhibited excellent cycling photostability in aqueous solution. The dispersion of CN-cy-Im was swiftly and repeatedly lightened by UV light for 50 ms at a time, maintaining nearly unchanged delayed emission patterns and intensities over 3000 cycles.

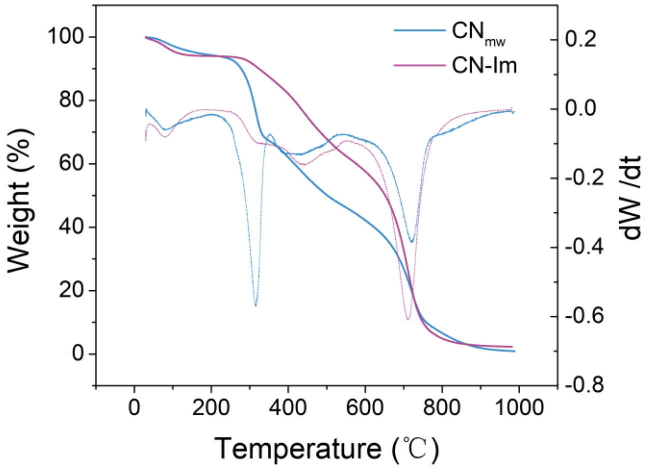

Fig. S13 TGA and derivative thermogravimetry curves of CN-cy-Im and CN$_{mw}$.

As shown in the Fig. S13, decomposition temperature of CN-cy-Im exceeded 300 ℃, indicating its good thermal stability. In contrast to CN$_{mw}$, the imidazolium salt dopant evidently improved the decomposition temperature and resulted in better thermal stability. This could be attributed to the fact that the further condensation of DCDA residues at higher temperatures was effectively hindered by covalent modification in accordance with the structural illustration of CN-cy-Im.

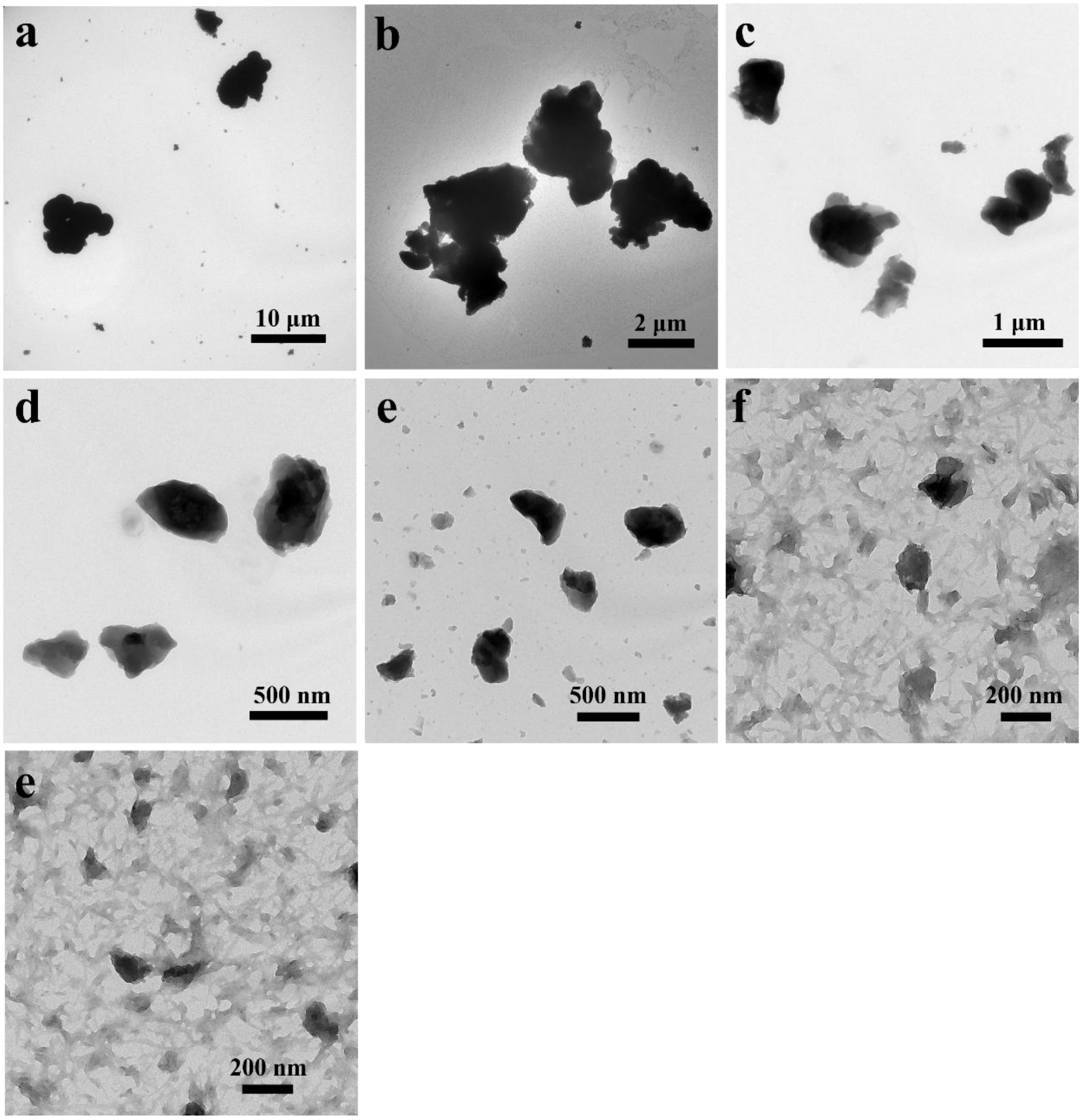

Fig. S14 TEM images of CN-cy-Im tailored into different particle size distributions of (a) 8000 nm, (b) 4000 nm, (c) 1000 nm, (d) 500 nm, (e) 350 nm, (f) 150 nm, (g) 60 nm.

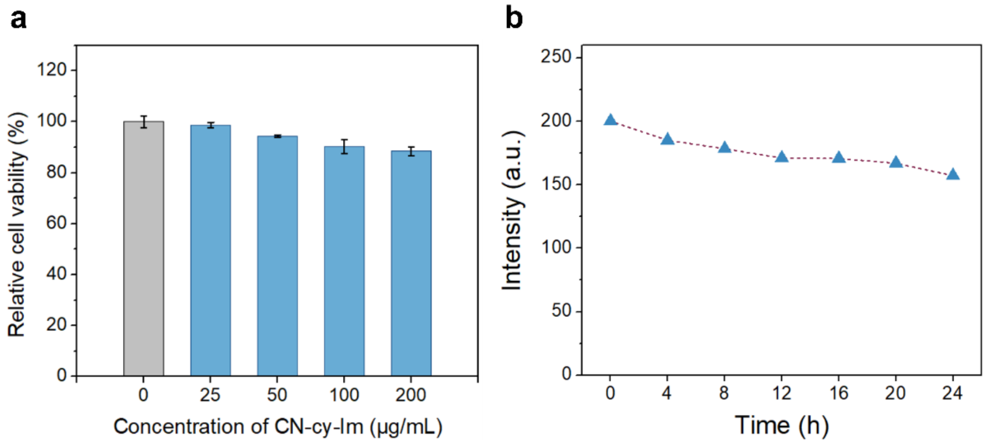

Fig. S15 (a) Cell viability of 4T1 cells after incubation with CN-cy-Im of multiple concentrations by CCK-8 assay. (b) Phosphorescence intensity of CN-cy-Im nanosheets (0.05 mg/mL) dispersed in DMEM cell culture medium for varying time intervals.

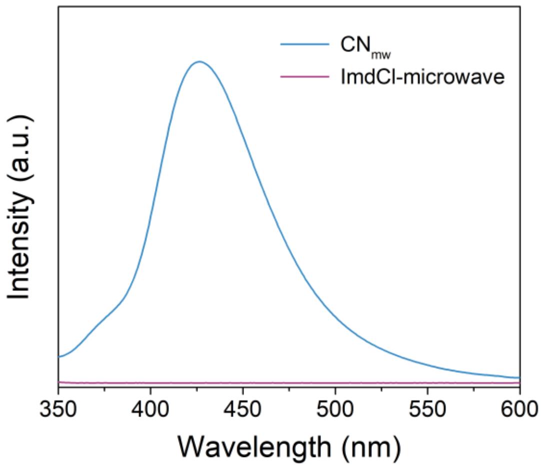

Fig. S16 Phosphorescence spectra of CN$_{mw}$ and microwave-treated imidazolium salt (ImdCl-microwave) (λ_{ex} = 330 nm).

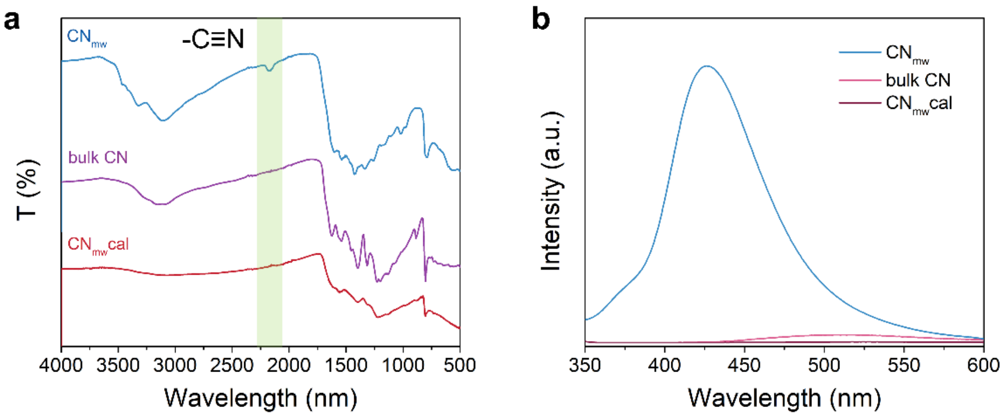

Fig. S17 (a) FT-IR spectra of CN$_{mw}$, bulk-CN, and CN$_{mw}$cal. (b) Phosphorescence spectra of CN$_{mw}$, bulk CN, and CN$_{mw}$cal with a delay time of 1ms.

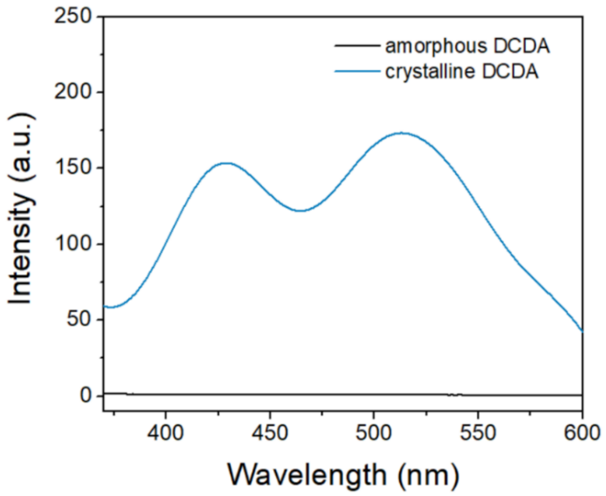

Fig. S18 Delayed emission spectra of DCDA in amorphous state and crystalline state (λ_{ex} = 330 nm).

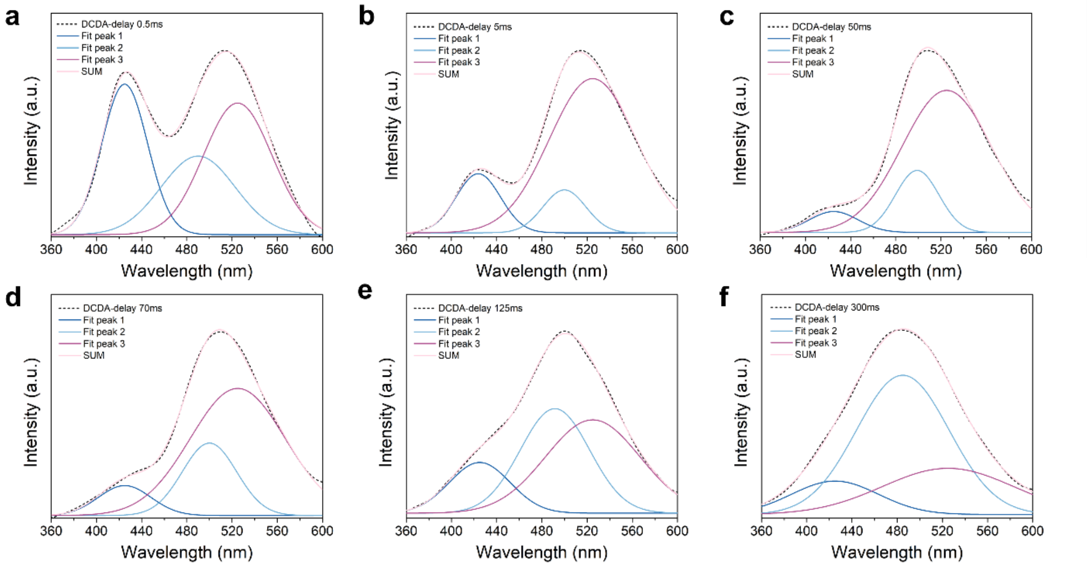

Fig. S19 Gaussian fittings for the steady-state photoluminescence spectrum of the DCDA crystal with various delay times of (a) 0.5 ms, (b) 5 ms, (c) 10 ms, (d) 50 ms, (e) 125 ms, and (f) 300 ms.

Gaussian fittings of phosphorescence spectra at different delay times revealed the existence of three stable emission centers (425, 485, and 525 nm) in crystalline DCDA with different lifetimes contributing to the total delayed luminescence.

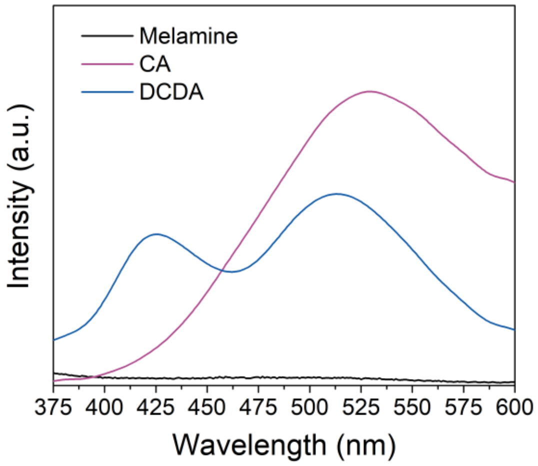

Fig. S20 Delayed emission spectra of the monomer (CA), dimer (DCDA), and trimer (melamine) with a delay time of 1 ms.

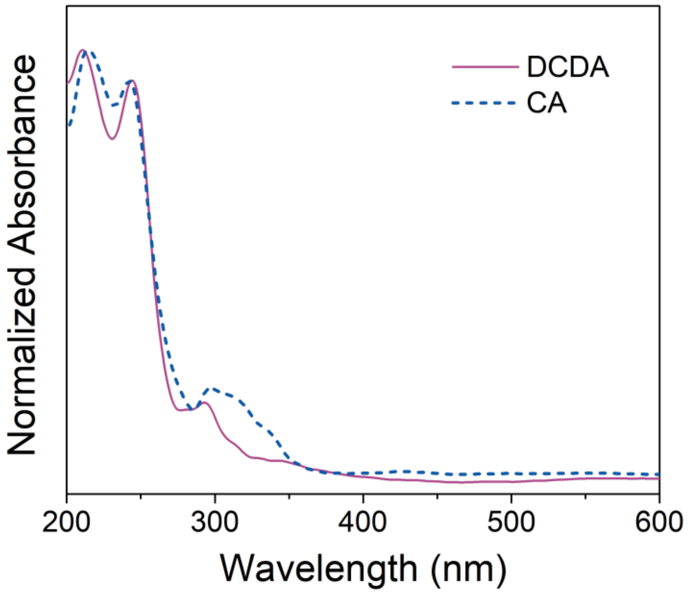

Fig. S21 UV-vis absorption spectra of CA and DCDA in the solid state.

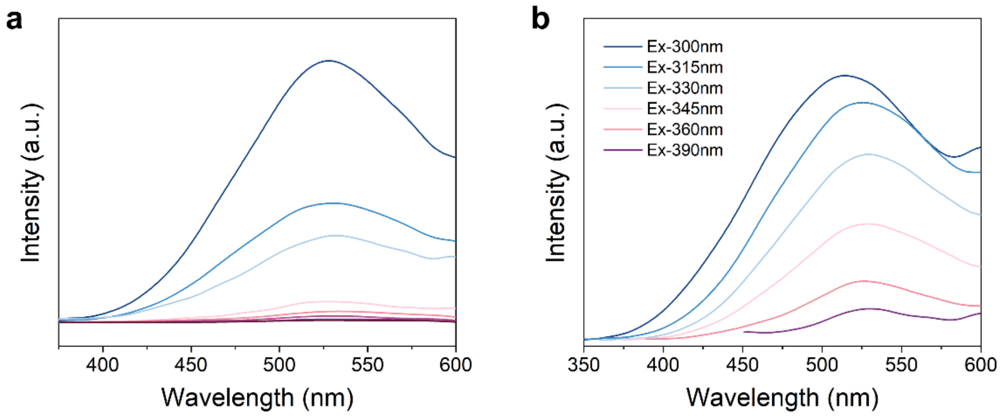

Fig. S22 Phosphorescence spectra of CA at (a) different delay times and (b) different excitation wavelengths.

In contrast to DCDA, the monomer CA, which has a simpler structure, exhibited a single emission band centered at 520 nm, regardless of the delay time (Fig. S20a) and the excitation wavelength (Fig. S20b), which could be ascribed to cyanide (C≡N) groups due to their unique n → π* transitions.

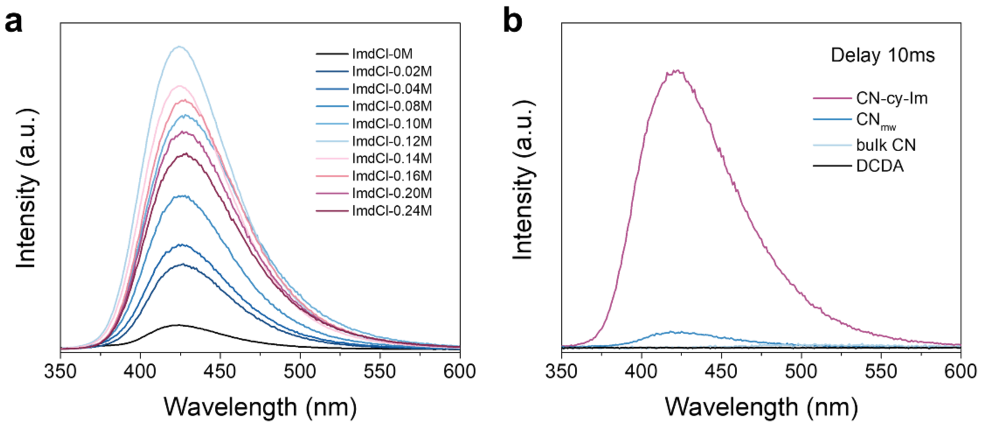

Fig. S23 (a) Phosphorescence intensity of CN-cy-Im functionalized with different concentrations of ImdCl. (b) Phosphorescence intensities of CN-cy-Im, CN$_{mw}$, bulk CN, and precursor DCDA at a delay time of 10 ms.

As shown in the Fig. S21a, the over-functionalization of ImdCl weakens the phosphorescence emission, which can be attributed to the excess reaction with the precursor, which probably interferes with the rigidity and integrity of the highly condensed CN skeleton, leading to more intense molecular vibration.

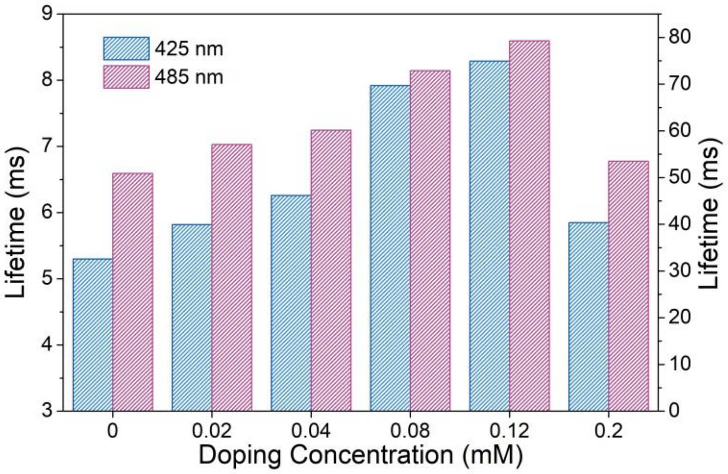

Fig. S24 Lifetime of CN-cy-Im with various doping concentrations at 425 nm (red bars) and 485 nm (blue bars)

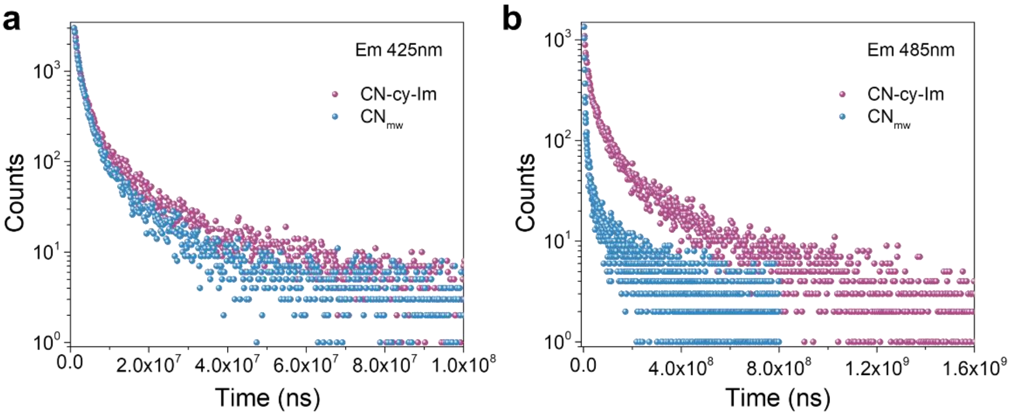

Fig. S25 Phosphorescence decay spectra of CN$_{mw}$ and CN-cy-Im at (a) 425 nm and (b) 485 nm.

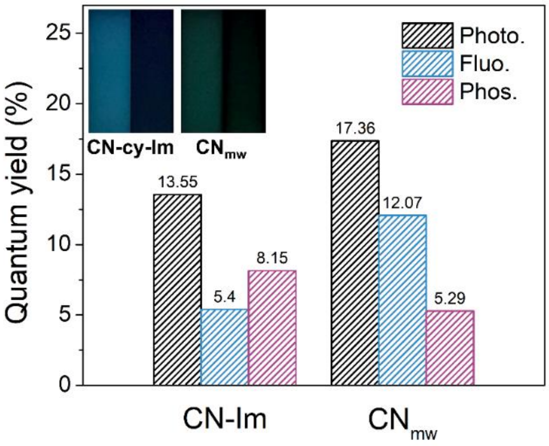

Fig. S26 Quantum yields of CN-cy-Im and CN$_{mw}$ in photoluminescence, fluorescence, and phosphorescence.

As shown in Fig. In S26, the absolute PQY in aqueous solution was improved by 2.86%, accompanied by an obvious enlargement of the phosphorescence portion in the Gaussian fittings of the photoluminescence spectra.

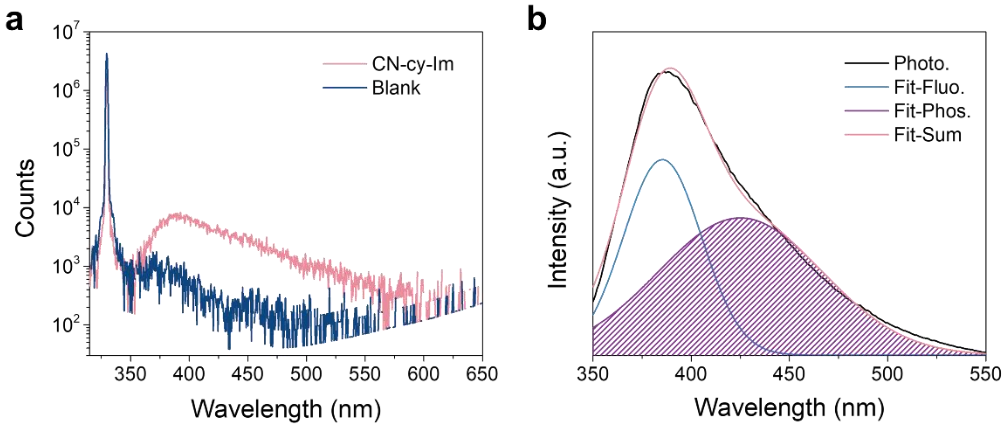

Fig. S27 (a) Photoluminescence quantum yield of CN-cy-Im in an aqueous solution. (b) Gaussian fittings for the steady-state photoluminescence spectrum of CN-cy-Im in aqueous solution. The shaded area was attributed to the emission of phosphorescence.

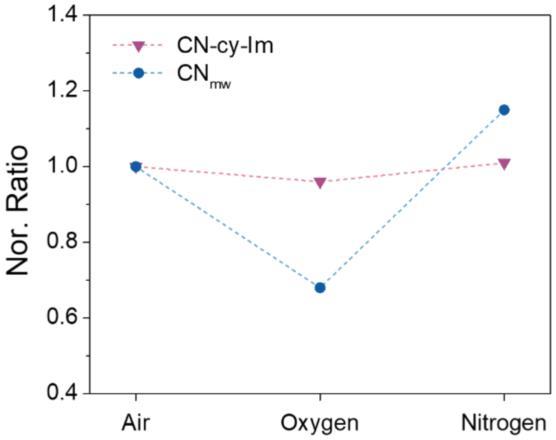

Fig. S28 Retention percentage of phosphorescence intensity of CN-cy-Im and CN$_{mw}$ in aqueous solution at different concentrations of oxygen, using air as the reference (λ_{ex} = 330 nm, delay time = 1 ms).

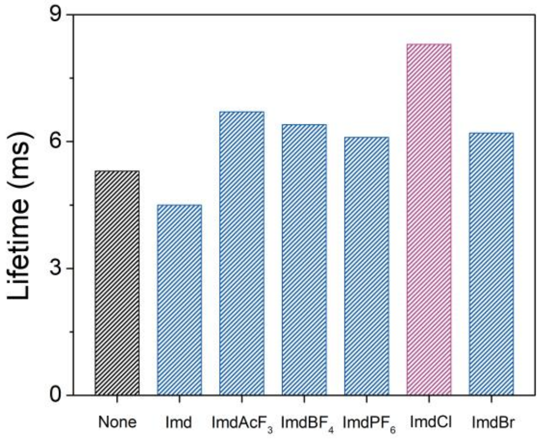

Fig. S29 Phosphorescence lifetimes of CN functionalized with imidazolium salts of various counter ions at 425 nm.

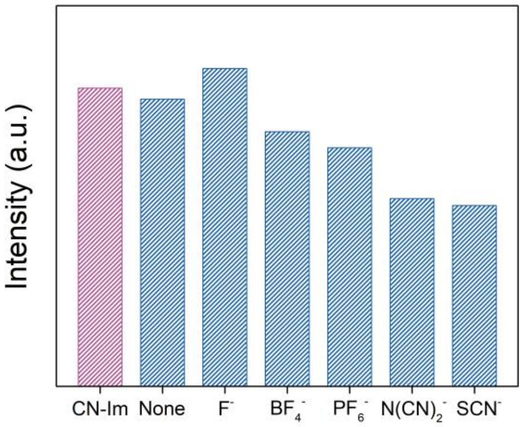

Fig. S30 Phosphorescence intensity of CN-cy-Im after ion-exchange with various anions.

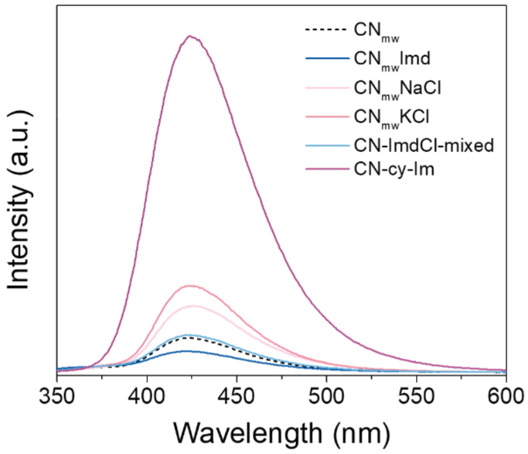

Fig. S31 Phosphorescence of a series of control samples in aqueous solution (0.5 mg/mL).

As illustrated in Fig. S31, the enhancement of aqueous RTP emission was scarcely noticeable in the sample created by merely physically blending the as-prepared CN$_{mw}$ with imidazolium ionic liquid at room temperature, compared to the one synthesized via microwave-assisted condensation. This suggests that covalent bonding is essential for improving the phosphorescence performance when dispersed in an aqueous solution. Additionally, the nitrogen cation of imidazolium was further confirmed as a crucial active site for such co-condensation with precursors, as evidenced by the minimal improvement in the aqueous RTP intensity when either chloride ions (Cl^-) or 1-butyl imidazole were added as a control.

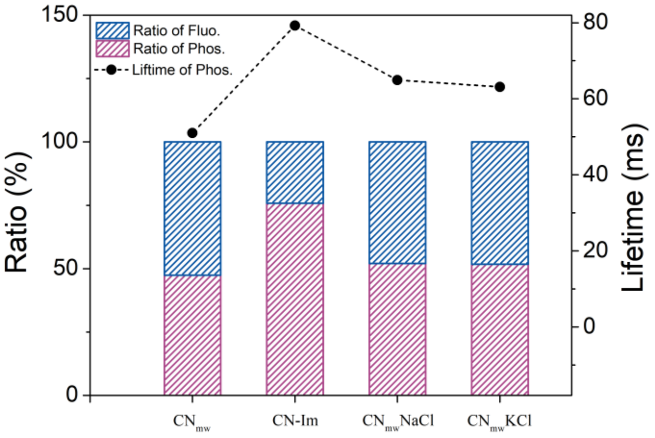

Fig. S32 Phosphorescence ratios in photoluminescence spectra and phosphorescence lifetimes of CN$_{mw}$, CN-cy-Im, CN$_{mw}$NaCl, and CN$_{mw}$KCl.

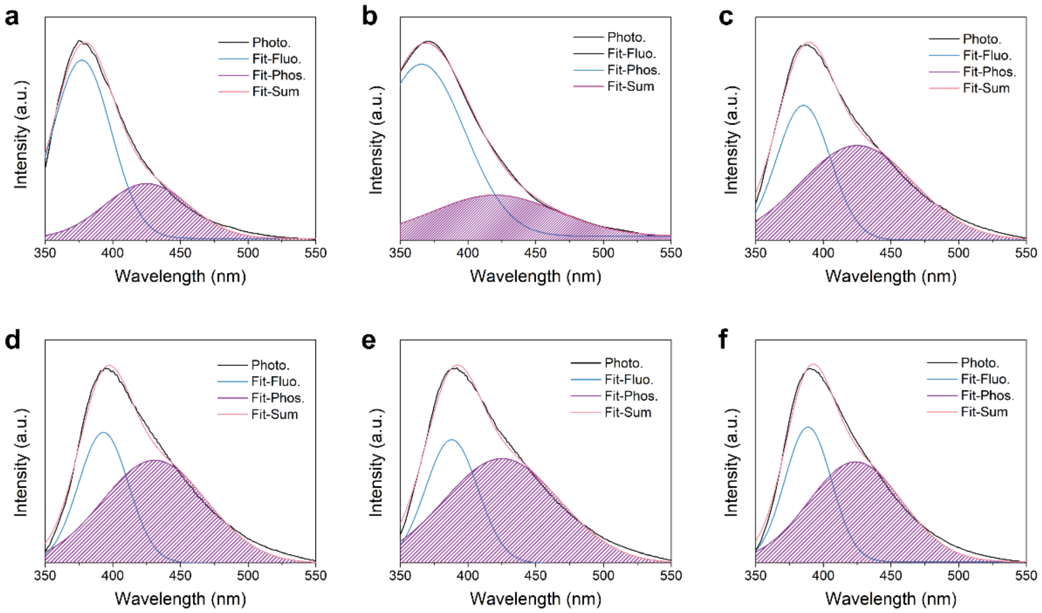

Fig. S33 Gaussian fittings for the steady-state photoluminescence spectra of (a) undoped CN$_{mw}$ and microwave-assisted CN functionalized with (b) Imd, (c) ImdCl, (d) ImdBF$_4$, (e) ImdPF$_6$ and (f) ImdBr.

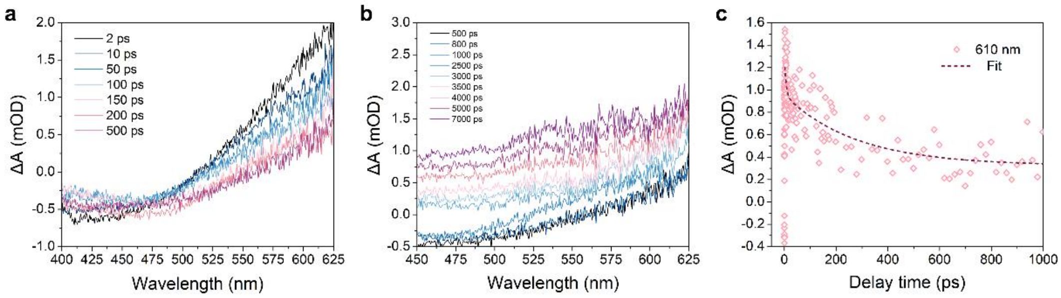

Fig. S34 fs-TA plots of CN-cy-Im in aqueous solution with excitation of 330 nm at different pump-probe delay times (a) from 2 ps to 500 ps and (b) from 500 ps to 7000 ps. (c) Representative ultrafast transient absorption kinetics of CN-cy-Im probed at 610 nm with excitation at 330 nm.

As illustrated in Fig. S34a, CN-cy-Im exhibited a negative absorption band from 400 to 500 nm under excitation at 330 nm, which was assigned to the integration of fluorescence and phosphorescence emissions. Specifically, the initial negative signal was primarily concentrated between 400-450 nm during a short delay period and then shifted to 450-500 nm as the delay time extended beyond 100 ps. This shift was predominantly influenced by stimulated and delayed emissions, as indicated by their respective emission spectra. More importantly, fs-TA plots at various delay times in a broader scope were measured and extracted to distinguish singlet and triplet excited states and further verify the existence of the ISC process. On one hand, it could be apparently observed that a broad positive absorption band ranging from 550 nm to 625 nm (incomplete peak pattern owing to limited testing range of the detector used) emerged within mere 2 ps and rapidly decreased as decay time prolonged to 500 ps, which was assigned to singlet excited-state absorption (ESA) in view of its fast kinetic decay at 610 nm (Fig. S34a and Fig. S34c). In contrast, with a further increase in the delay time from 500 ps to 7000 ps, a positive absorption newly appeared ranging from 525 to 600 nm was gradually increased, implying a longer lifetime than the decay ones, which could be assigned to the triplet ESA (Fig. S34b).

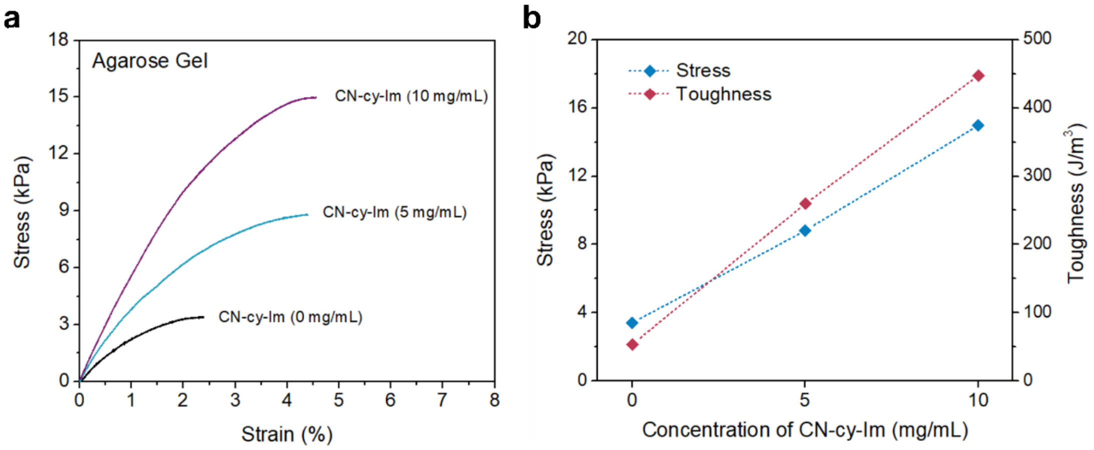

Fig. S35 (a) Stress-strain curves of agarose hydrogel with multiple concentrations of CN-cy-Im (b) Comparison of both stress and toughness for agarose hydrogel mixed with varying concentration of CN-cy-Im.

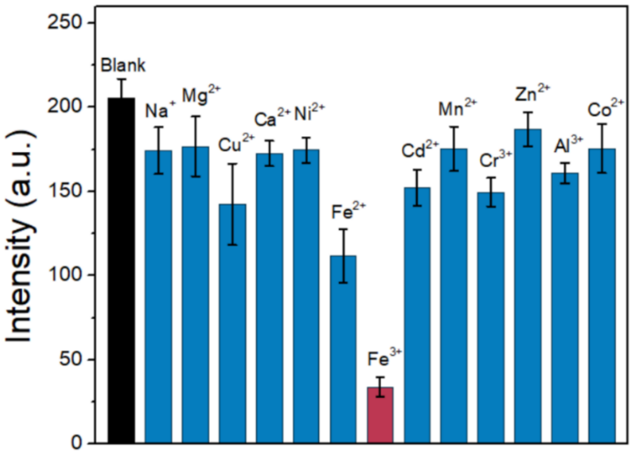

Fig. S36 Afterglow intensity of CN-cy-Im hydrogel with addition of multiple metal ions (100 μM) in aqueous solution (λ_{ex} = 330 nm, delay time = 1 ms).

As illustrated in Fig. S36, the phosphorescence response test for various metal ions revealed that CN-cy-Im was selectively quenched by Fe^{3+} in an aqueous solution.

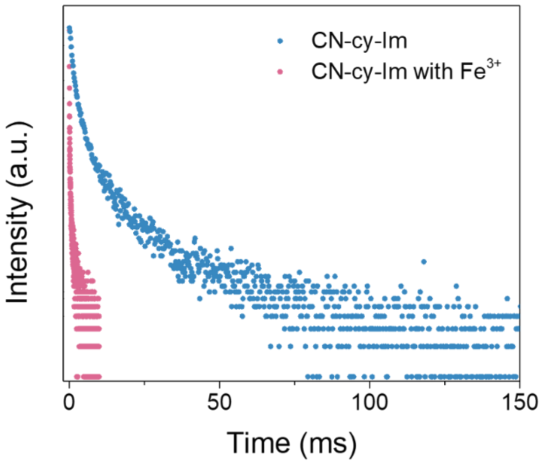

Fig. S37 Phosphorescence decay spectra of CN-cy-Im before and after quenching by Fe^{3+} in an aqueous solution.

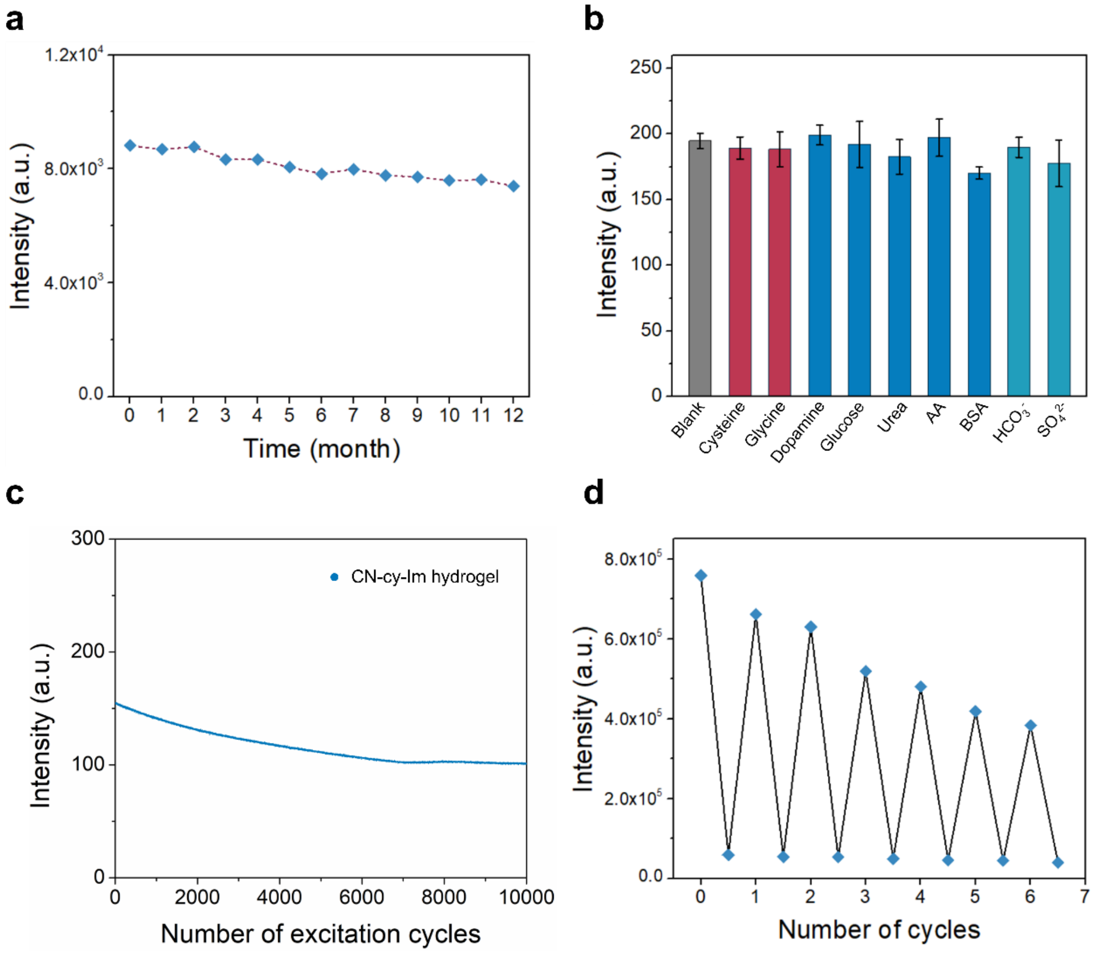

Fig. S38 (a) Afterglow intensity of RTP hydrogel after storage at room-temperature for different durations. (b) Afterglow intensity of RTP hydrogel when mixed with multiple biological interferents (100 μM). (c) Afterglow intensity of RTP hydrogel under cyclic excitation (λ_{ex} = 330 nm) (d) Variation of hydrogel afterglow intensity with alternate addition of aqueous Fe^{3+} (300 μM) and EDTA-2Na solution (500 μM).

Table S1. Combustion elemental analyses of CN_{mw} and CN-cy-Im.

Sample	C [wt.%]	N [wt.%]	H[wt.%]	C/N [molar ratio]
CN_{mw}	30.8	55.58	4.61	0.6465
CN-cy-Im	30.42	55.16	3.96	0.6434

Table S2. Comparation of existing metal-free aqueous RTP materials in literature.

Material	Method	Lifetime (ms)	PQY (%)	Ref.
G⊂CB[7]@HACD	Matrix-assisted	0.581	14.96	[11]
HOF@NPA	Matrix-assisted	4.91	2.18	[12]
1/CB[8]	Matrix-assisted	110.2	99.38	[13]
CNDs@CA	Matrix-assisted	951.25	26.89	[14]
G-CDs@SiO2	Matrix-assisted	1500	11.08	[15]
BBA/α-CD	Matrix-assisted	16.75	63.48	[16]
AQPY⊂CB[8]	Matrix-assisted	0.376	1.53	[17]
G⊂LP@PAAm	Matrix-assisted	4.2	21.93	[18]
TBBP-CB[8]	Matrix-assisted	0.451	2.3	[19]
PACs-B_2O_3	Matrix-assisted	2138	15.87	[20]
2-NA@HOFs	Matrix-assisted	493.1	32.09	[21]
p-N-DPC$(PF_6)_2$	Crystalline	0.42	N.A.	[22]
Rh(I) complexe	Crystalline	0.008	3.93	[23]
C4-I	Crystalline	3.3	3.1	[24]
BrNPs	Crystalline	0.028	N.A.	[25]
Pyrene-d_{10}	Crystalline	4	26.9	[26]
PDPy/TPA	Crystalline	139	N.A.	[27]
CN-cy-Im	Trinity Strategy	79.8	8.15	This work

Table S3. Quantum yields and Phosphorescence ratios of CN_{mw} doped with various anions.

	Photo. QY	Fluo.Ratio	Phos. Ratio	Fluo. QY	Phos. QY
CN_{mw}	17.36%	69.49%	30.51%	12.07%	5.29%
CN-cy-Im	13.55%	39.87%	60.13%	5.40%	8.15%
CN-cy-ImdBr	11.73%	43.84%	56.16%	5.14%	6.59%
CN-cy-Imd AcF_3	7.72%	40.96%	59.04%	3.16%	4.56%
CN-cy-Imd BF_4	10.83%	38.11%	61.89%	4.13%	6.70%

CN-cy-Imd PF_6	6.62%	36.15%	63.85%	2.23%	4.23%

Table S4. Dynamic photophysical parameters of CN_{mw} and CN-cy-Im.

Sample	τ_F	Φ_F	τ_P	Φ_P	k_r^F	Φ_{ISC}	k_{ISC}	k_r^P	k_{nr}^P
	[ns]	[%]	[ms]	[%]	[s^{-1}]	[%]	[s^{-1}]	[s^{-1}]	[s^{-1}]
CN_{mw}	13.86	12.07	5.37	5.29	8.71×10^6	89.73	3.82×10^6	9.85	176.37
CN-cy-Im	12.34	5.40	8.29	8.15	4.38×10^6	94.60	6.72×10^6	9.83	110.79

$k_r^F = \Phi_F / \tau F$; $k_r^P = \Phi_P / \tau P$; $k_{ISC} = \Phi_P / \tau_F$; $k_{nr}^P = (1-\Phi_F-\Phi_P) / \tau_F$

Table S5. Comparation of existing optical detection methods for Fe^{3+} in literature.

Material	Method	Linear range (μM)	LOD (μM)	Ref.
BP AIEgens	fluorescence	0.5-50	0.016	[28]
Ni-CDs	fluorescence	0.1-70	0.051	[29]
TiC-CQDs	fluorescence	5-60	0.14	[30]
CQDs-PEGDA	fluorescence	0-250	0.6	[31]
Poly(ethylene glycol)	fluorescence	0-60	0.99	[32]
LG-CS@SeNPs	fluorescence	5-250	2.3	[33]
PAA@CDs	fluorescence	50-2600	5.14	[34]
TPA-Bp	fluorescence	40-320	10.2	[35]
BNS-CDs	colorimetry	0.3-546	0.09	[36]
UiO-66-$(OH)_2$	colorimetry	5-60	1.26	[37]
PDA-Im	colorimetry	10-200	9	[38]
N,S-CDs	colorimetry	75-675	20	[39]
BTPY@ns-Q[10]	afterglow	2-12	0.49	[40]
PLNPs@PDA	afterglow	10-800	2.86	[41]
CuO nanozyme@PLNPs	afterglow	0-700	3.76	[42]
CDs@pRHO	afterglow	0-500	9.8	[43]
CN-cy-Im	afterglow	10-300	3.02	This work

Table S6. Recovery results of Fe^{3+} detection in human serum.

Sample	Spiked Fe^{3+} (μM)	Found (μM)	Recovery (%)	RSD (%, n=3)
1	20	22.29	111.46%	0.81%
2	80	74.99	93.74%	8.35%
3	140	140.53	100.38%	4.18%
4	200	191.48	95.74%	9.56%
5	260	257.91	99.20%	8.93%

3. References

1. Wang, B.; Yu, Y.; Zhang, H.; Xuan, Y.; Chen, G.; Ma, W.; Li, J.; Yu, J., Carbon Dots in a Matrix: Energy-Transfer-Enhanced Room-Temperature Red Phosphorescence. *Angew. Chem. Int. Ed.* **2019,** *58*, 18443-18448.
2. Li, J.; Zhou, H.; Jin, S.; Xu, B.; Teng, Q.; Li, C.; Li, J.; Li, Q.; Gao, Z.; Zhu, C.; Wang, Z.; Su, W.; Yuan, F., Achieving Bright and Long‐Lived Aqueous Room-Temperature Phosphorescence of Carbon Nitrogen Dots Through In Situ Host-Guest Binding. *Adv. Mater.* **2024,** *36*, 2401493.
3. Peng, H.; Xie, G.; Cao, Y.; Zhang, L.; Yan, X.; Zhang, X.; Miao, S.; Tao, Y.; Li, H.; Zheng, C.; Huang, W.; Chen, R., On-demand modulating afterglow color of water-soluble polymers through phosphorescence FRET for multicolor security printing. *Sci. Adv.* **2022,** *8*, eabk2925.
4. Frisch, M. J.; Trucks, G. W.; Schlegel, H. B.; Scuseria, G. E.; Robb, M. A.; Cheeseman, J. R.; Scalmani, G.; Barone, V.; Petersson, G. A.; Nakatsuji, H.; Li, X.; Caricato, M.; Marenich, A. V.; Bloino, J.; Janesko, B. G.; Gomperts, R.; Mennucci, B.; Hratchian, H. P.; Ortiz, J. V.; Izmaylov, A. F.; Sonnenberg, J. L.; Williams; Ding, F.; Lipparini, F.; Egidi, F.; Goings, J.; Peng, B.; Petrone, A.; Henderson, T.; Ranasinghe, D.; Zakrzewski, V. G.; Gao, J.; Rega, N.; Zheng, G.; Liang, W.; Hada, M.; Ehara, M.; Toyota, K.; Fukuda, R.; Hasegawa, J.; Ishida, M.; Nakajima, T.; Honda, Y.; Kitao, O.; Nakai, H.; Vreven, T.; Throssell, K.; Montgomery Jr., J. A.; Peralta, J. E.; Ogliaro, F.; Bearpark, M. J.; Heyd, J. J.; Brothers, E. N.; Kudin, K. N.; Staroverov, V. N.; Keith, T. A.; Kobayashi, R.; Normand, J.; Raghavachari, K.; Rendell, A. P.; Burant, J. C.; Iyengar, S. S.; Tomasi, J.; Cossi, M.; Millam, J. M.; Klene, M.; Adamo, C.; Cammi, R.; Ochterski, J. W.; Martin, R. L.; Morokuma, K.; Farkas, O.; Foresman, J. B.; Fox, D. J. *Gaussian 16 Rev. C.01*, Wallingford, CT, 2016.
5. Zhao, Y.; Truhlar, D. G., The M06 suite of density functionals for main group thermochemistry, thermochemical kinetics, noncovalent interactions, excited states, and transition elements: two new functionals and systematic testing of four M06-class functionals and 12 other functionals. *Theor. Chem. Acc.* **2007,** *120*, 215-241.
6. Lu, T.; Chen, F., Multiwfn: A multifunctional wavefunction analyzer. *J. Comput. Chem.* **2011,** *33*, 580-592.
7. Humphrey, W.; Dalke, A.; Schulten, K., VMD: Visual molecular dynamics. *Journal of Molecular Graphics* **1996,** *14*, 33-38.
8. Zhou, Z.; Wang, J.; Yu, J.; Shen, Y.; Li, Y.; Liu, A.; Liu, S.; Zhang, Y., Dissolution and Liquid Crystals Phase of 2D Polymeric Carbon Nitride. *J. Am. Chem. Soc.* **2015,** *137*, 2179-2182.
9. Huang, C.; Wen, Y.; Ma, J.; Dong, D.; Shen, Y.; Liu, S.; Ma, H.; Zhang, Y., Unraveling fundamental active units in carbon nitride for photocatalytic oxidation reactions. *Nat. Commun.* **2021,** *12*, 320.
10. Yu, H.; Shi, R.; Zhao, Y.; Bian, T.; Zhao, Y.; Zhou, C.; Waterhouse, G. I. N.; Wu, L. Z.; Tung, C. H.; Zhang, T., Alkali‐Assisted Synthesis of Nitrogen Deficient Graphitic Carbon Nitride with Tunable Band Structures for Efficient Visible‐Light‐Driven Hydrogen Evolution. *Adv. Mater.* **2017,** *29*, 1605148.

11. Dai, X. Y.; Huo, M.; Dong, X.; Hu, Y. Y.; Liu, Y., Noncovalent Polymerization‐Activated Ultrastrong Near‐Infrared Room‐Temperature Phosphorescence Energy Transfer Assembly in Aqueous Solution. *Adv. Mater.* **2022,** *34*, 2203534.

12. Xia, Q. Q.; Yu, J. L.; Chen, Z. Y.; Xue, Z. Y.; Wang, X. H.; Liu, X.; Wu, M. X., High-performance room temperature phosphorescence prompted by hydrogen-bonded organic frameworks. Cell Rep. Phys. Sci. **2023,** *4*, 101494.

13. Ma, X. K.; Zhang, W.; Liu, Z.; Zhang, H.; Zhang, B.; Liu, Y., Supramolecular Pins with Ultralong Efficient Phosphorescence. *Adv. Mater.* **2021,** *33*, 2007476.

14. Li, J.; Zhou, H.; Jin, S.; Xu, B.; Teng, Q.; Li, C.; Li, J.; Li, Q.; Gao, Z.; Zhu, C.; Wang, Z.; Su, W.; Yuan, F., Achieving Bright and Long ‐ Lived Aqueous Room‐Temperature Phosphorescence of Carbon Nitrogen Dots Through In Situ Host-Guest Binding. *Adv. Mater.* **2024,** *36*, 2401493.

15. Liao, J.; Chen, X.; Li, J.; Gong, X., Engineering strategy for achieving transparent aqueous multicolor long lifetime room temperature phosphorescent carbon dots. *Nano Energy* **2025,** *146, 111532.*

16. Bai, X.; Song, Q.; Yang, S.; Ge, Y.; Dai, X. Y., Time‐Evolving Aqueous Organic Room‐Temperature Phosphorescence from a Native Cyclodextrin‐Based Supramolecular Co‐Assembly. *Adv. Opt. Mater.* **2025,** *13*, e02379.

17. Yu, H. J.; Zhou, Q.; Dai, X.; Shen, F. F.; Zhang, Y. M.; Xu, X.; Liu, Y., Photooxidation-Driven Purely Organic Room-Temperature Phosphorescent Lysosome-Targeted Imaging. *J. Am. Chem. Soc.* **2021,** *143*, 13887-13894.

18. Song, Q.; Liu, Z.; Li, J.; Sun, Y.; Ge, Y.; Dai, X. Y., Achieving Near‐Infrared Phosphorescence Supramolecular Hydrogel Based on Amphiphilic Bromonaphthalimide Pyridinium Hierarchical Assembly. *Adv. Mater.* **2024,** *36*, 2409983.

19. Yin, C.; Yan, Z. A.; Yan, R.; Xu, C.; Ding, B.; Ji, Y.; Ma, X., A 3D Phosphorescent Supramolecular Organic Framework in Aqueous Solution. *Adv. Funct. Mater.* **2024,** *34*, 2316008.

20. Ding, Y.; Yang, C.; Gan, F.; Zhang, G.; Shen, C.; Qiu, H., Ultrahigh-Temperature Long-Persistent Luminescence from B_2O_3-Confined Polycyclic Aromatic Compounds. *J. Am. Chem. Soc.* **2024,** *146*, 25211-25220.

21. Luo, W.; Zhou, J.; Nie, Y.; Li, F.; Cai, S.; Yin, G.; Chen, T.; Cai, Z., Hydrogen‐Bonded Organic Frameworks Enabling Highly Robust Aqueous Phase Ultralong Room‐Temperature Phosphorescence. *Adv. Funct. Mater.* **2024,** *34*, 2401728.

22. Zhou, Q.; Liu, Y.; Ma, X.; Fan, W.; Cheng, Y.; He, R.; Meng, X.; Shi, Y.; Cao, Q.; Zheng, L., Luminophore with Multiple Emission Centers for Fluorescence/ Phosphorescence Dual Ratiometric Chemical Sensing in Aqueous Solution. *Adv. Opt. Mater.* **2024,** *12*, 2303107.

23. Shi, B.; Zhang, L.; Yan, K.; Ming, J.; Chen, Z. H.; Chen, Y.; He, H.; Zhang, H.; Wang, L.; Wang, S.; Zhang, F., Efficient and Stable NIR ‐ II Phosphorescence of Metallophilic Molecular Oligomers for In Vivo Single‐Cell Tracking and Time‐Resolved Imaging. *Angew. Chem. Int. Ed.* **2024,** *63,* e202410118.

24. Wang, X. F.; Guo, W. J.; Xiao, H.; Yang, Q. Z.; Chen, B.; Chen, Y. Z.; Tung, C. H.; Wu, L. Z., Pure Organic Room Temperature Phosphorescence from Unique Micelle‐Assisted Assembly of Nanocrystals in Water. *Adv. Funct. Mater.* **2020,** *30*, 1907282.

25. Wang, X. F.; Xiao, H.; Chen, P. Z.; Yang, Q. Z.; Chen, B.; Tung, C. H.; Chen, Y. Z.; Wu,

L. Z., Pure Organic Room Temperature Phosphorescence from Excited Dimers in Self-Assembled Nanoparticles under Visible and Near-Infrared Irradiation in Water. *J. Am. Chem. Soc.* **2019,** *141*, 5045-5050.

26. Abe, A.; Goushi, K.; Mamada, M.; Adachi, C., Organic Binary and Ternary Cocrystal Engineering Based on Halogen Bonding Aimed at Room‐Temperature Phosphorescence. *Adv. Mater.* **2023,** *36*, 2211160.

27. Dai, W.; Zhang, Y.; Wu, X.; Guo, S.; Ma, J.; Shi, J.; Tong, B.; Cai, Z.; Xie, H.; Dong, Y., Red-Emissive Organic Room-Temperature Phosphorescence Material for Time-Resolved Luminescence Bioimaging. *CCS Chemistry* **2022,** *4*, 2550-2559.

28. Zheng, H.; Ma, H.; Sun, H.; Zhang, L.; Zhang, X.; Sun, R.; Wang, H.; Xu, G. Y.; Wang, L.; Qi, Y., Rapid and accurate identification of multiple metal ions using a bispyrene‐based fluorescent sensor array with aggregation‐induced enhanced emission property. *Aggregate* **2024,** *6*, e678.

29. Huang, S.; Zhang, W.; Li, B.; Li, G.; Ni, W.; Fang, Y.; Xiao, Q., An innovative red-emitting nickel-doped carbon dot for simultaneous detection of Fe(III) and pyrophosphate ions, coupled with synergistic photothermal/photodynamic cancer therapy. *Anal. Chim. Acta* **2025,** *1360, 344138*.

30. Wang, W.; Bai, X.; Zhou, H.; Shan, J.; Wang, X., Energy-Efficient, Room-Temperature, and Facile Synthesis of Carbon Quantum Dots from Interstitial Compound TiC for the Selective Detection of Fe(III). ACS Sustain. Chem. Eng. **2023,** *11*, 14133-14143.

31. Cai, Y.; Zhang, J.; Zhang, M.; Wang, M.; Zhao, Y., The optical fiber sensing platform for ferric ions detection: A practical application for carbon quantum dots. Sens. Actuators B Chem. **2022,** *364,* 131857.

32. Sun, C.; Jiang, X.; Li, B.; Li, S.; Kong, X. Z., Fluorescence Behavior and Mechanisms of Poly(ethylene glycol) and Their Applications in Fe^{3+} and Cr^{6+} Detections, Data Encryption, and Cell Imaging. ACS Sustain. Chem. Eng. **2021,** *9*, 5166-5178.

33. Wang, Y. r.; Li, D. h.; Shi, Y.; Li, Y. q.; Chen, R. k.; Wang, Z. r.; Zhang, C.; Jiang, B.; Wen, Y. y.; Tong, J. p.; Shi, Y. g.; Shen, Y.; Ettelaie, R.; Gu, Q., A Green Photoregulated Quadruple‐Action Selenium Nanozyme Platform for Rapid and Ferroptosis‐Like‐Enhanced Photodynamic Bacterial Killing with Integrated Biosensing Capabilities. *Small* **2025,** *22*, e10654.

34. Zhou, Y.; Li, H.; Gu, J.; Fu, Y.; Liu, J.; Li, Z.; Li, X.; Liu, X.; Qiao, Z.; Liu, Y., Construction of a Fluorescence/Phase-Change Dual-Mode Sensor Based on Carbon Dots/Poly(acrylic acid) for Highly Selective and Sensitive Detection of Ferric Ions. ACS Appl. Mater. Interfaces **2024,** *16*, 61036-61049.

35. Zhang, C.; Pan, G.; He, Y., Conjugated microporous organic polymer as fluorescent chemosensor for detection of Fe3+ and Fe2+ ions with high selectivity and sensitivity. *Talanta* **2022,** *236, 122872*.

36. Liu, Y.; Duan, W.; Song, W.; Liu, J.; Ren, C.; Wu, J.; Liu, D.; Chen, H., Red Emission B, N, S-co-Doped Carbon Dots for Colorimetric and Fluorescent Dual Mode Detection of Fe^{3+} Ions in Complex Biological Fluids and Living Cells. ACS Appl. Mater. Interfaces **2017,** *9*, 12663-12672.

37. Wang, H.; Wang, X.; Kong, R. M.; Xia, L.; Qu, F., Metal-organic framework as a multi-component sensor for detection of Fe3+, ascorbic acid and acid phosphatase. *Chin. Chem.*

Lett. **2021,** *32*, 198-202.
38. Shin, H.; Jannah, F.; Yoo, E. J.; Kim, J.-M., A colorimetric and fluorescence “turn-on” sensor for Fe(III) ion based on imidazole-functionalized polydiacetylene. Sens. Actuators B Chem. **2022,** *350, 130885*.
39. Amiri, M.; Haji Shabani, A. M.; Dadfarnia, S.; Shokoufi, N.; Hajipour-Verdom, B.; Sadjadi, S., Carbon dots doped by nitrogen and sulfur for dual-mode colorimetric and fluorometric determination of Fe^{3+} and histidine and intracellular imaging of Fe^{3+} in living cells. *Microchimica Acta* **2020,** *187*, 562.
40. Cen, R.; Liu, M.; Liu, C.; Leng, Q. H.; Ren, Q.; Tao, Z.; Xiao, X., nor-seco-Cucurbit[10]uril-based Supramolecular Assembly for Ultralong Afterglow Room-Temperature Phosphorescence Material and Metal Ion Detection. *ACS Mater. Lett.* **2024,** *6*, 1992-1998.
41. Jia, B.; Long, Z.; Liu, X.; Feng, B.; Zhang, P.; Qing, T., Persistent luminescent nanoparticles with enhanced afterglow through polydopamine modification for separation-free and visual detection of iron ions in water. *Microchem. J.* **2024,** *207, 111943*.
42. Guo, X. H.; Abdurahman, R.; Guan, M.; Zhang, Y.; Yin, X. B.; Gao, J.; Wu, S. Q., Enzyme activity-enhanced persistent luminescent nanoparticle Nanozyme composite based smart paper Chip sensor for immediate detection of Fe^{3+} and cholesterol. *Microchem. J.* **2025,** *218, 115665*.
43. Zong, S.; Yu, X.; Yang, Y.; Yang, X.; Li, J., Multi-mode luminescence anti-counterfeiting and visual iron(Ⅲ) ions RTP detection constructed by assembly of CDs&Eu^{3+} in porous RHO zeolite. *Chin. Chem. Lett.* **2025,** *36*, 110343.